

EXPERIENCE THE FUTURE OF ADVANCED  
PRECISION QA AT AAPM IN NASHVILLE

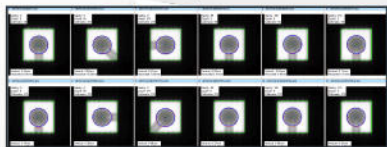


AAPM 2018 // BOOTH #1033

Be the first to  
demo the latest and  
greatest innovations in  
quality assurance solutions  
with RIT's new software upgrade:

## RIT VERSION 6.7.X

GIBBS CONE ANALYSIS



SUB-PIXEL ACCURACY  
ISOCENTER OPTIMIZATION

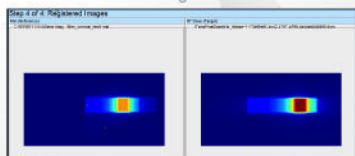
STREAMLINED  
WORKFLOW &  
USER INTERFACE

ELEKTA  
LEAF SPEED  
ANALYSIS

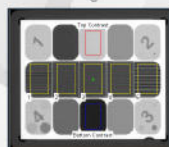
NEW SOFTWARE  
LICENSE MANAGEMENT

CUSTOM  
AND DEFAULT  
TOLERANCE  
MANAGER

  
**Cerberus**  
VERSION 2.0:  
COMPLETE IMAGING QA  
AUTOMATION



TOMOTHERAPY® REGISTRATION  
FOR PATIENT QA



QC-kV1  
PHANTOM  
ANALYSIS

SEE MORE AT  
**BOOTH #1033**

Tomotherapy® is a registered trademark of Accuray, Inc.

## THE RIT BREAKFAST SEMINAR

Don't miss the most  
important meal of  
AAPM 2018!

**JULY 29, 2018**  
**7:00-9:00 AM**  
THE OMNI NASHVILLE HOTEL  
BROADWAY BALLROOMS A/B

**CLICK HERE TO  
RESERVE A SPOT**

(Space is limited, and a  
reservation is required.)

The RIT Family of Products: Medical Physics' Leading QA Software for Over 25 Years

Connect with RIT  
**@RIT4QA**



**RADIMAGE.COM**

(+1) 719-590-1077 // sales@radimage.com

©2018, Radiological Imaging Technology, Inc.

# Lung morphometry using hyperpolarized $^{129}\text{Xe}$ multi- $b$ diffusion MRI with compressed sensing in healthy subjects and patients with COPD

Huiting Zhang

*School of Physics, Huazhong University of Science and Technology, Wuhan 430074, China*

*State Key Laboratory of Magnetic Resonance and Atomic and Molecular Physics, National Center for Magnetic Resonance in Wuhan, Wuhan Institute of Physics and Mathematics, Chinese Academy of Sciences, Wuhan 430071, China*

Junshuai Xie, Sa Xiao, Xiuchao Zhao, Ming Zhang, and Lei Shi

*State Key Laboratory of Magnetic Resonance and Atomic and Molecular Physics, National Center for Magnetic Resonance in Wuhan, Wuhan Institute of Physics and Mathematics, Chinese Academy of Sciences, Wuhan 430071, China*

Ke Wang and Guangyao Wu

*Department of Magnetic Resonance Imaging, Zhongnan Hospital of Wuhan University, Wuhan 430071, China*

Xianping Sun

*State Key Laboratory of Magnetic Resonance and Atomic and Molecular Physics, National Center for Magnetic Resonance in Wuhan, Wuhan Institute of Physics and Mathematics, Chinese Academy of Sciences, Wuhan 430071, China*

Chaohui Ye

*School of Physics, Huazhong University of Science and Technology, Wuhan 430074, China*

*State Key Laboratory of Magnetic Resonance and Atomic and Molecular Physics, National Center for Magnetic Resonance in Wuhan, Wuhan Institute of Physics and Mathematics, Chinese Academy of Sciences, Wuhan 430071, China*

Xin Zhou<sup>a)</sup>

*State Key Laboratory of Magnetic Resonance and Atomic and Molecular Physics, National Center for Magnetic Resonance in Wuhan, Wuhan Institute of Physics and Mathematics, Chinese Academy of Sciences, Wuhan 430071, China*

(Received 6 July 2017; revised 18 April 2018; accepted for publication 19 April 2018; published 20 May 2018)

**Purpose:** To demonstrate the feasibility of compressed sensing (CS) to accelerate the acquisition of hyperpolarized (HP)  $^{129}\text{Xe}$  multi- $b$  diffusion MRI for quantitative assessments of lung microstructural morphometry.

**Methods:** Six healthy subjects and six chronic obstructive pulmonary disease (COPD) subjects underwent HP  $^{129}\text{Xe}$  multi- $b$  diffusion MRI ( $b = 0, 10, 20, 30,$  and  $40 \text{ s/cm}^2$ ). First, a fully sampled (FS) acquisition of HP  $^{129}\text{Xe}$  multi- $b$  diffusion MRI was conducted in one healthy subject. The acquired FS dataset was retrospectively undersampled in the phase encoding direction, and an optimal twofold undersampled pattern was then obtained by minimizing mean absolute error (MAE) between retrospective CS (rCS) and FS MR images. Next, the FS and CS acquisitions during separate breath holds were performed on five healthy subjects (including the above one). Additionally, the FS and CS synchronous acquisitions during a single breath hold were performed on the sixth healthy subject and one COPD subject. However, only CS acquisitions were conducted in the rest of the five COPD subjects. Finally, all the acquired FS, rCS and CS MR images were used to obtain morphometric parameters, including acinar duct radius ( $R$ ), acinar lumen radius ( $r$ ), alveolar sleeve depth ( $h$ ), mean linear intercept ( $L_m$ ), and surface-to-volume ratio (SVR). The Wilcoxon signed-rank test and the Bland–Altman plot were employed to assess the fidelity of the CS reconstruction. Moreover, the  $t$ -test was used to demonstrate the effectiveness of the multi- $b$  diffusion MRI with CS in clinical applications.

**Results:** The retrospective results demonstrated that there was no statistically significant difference between rCS and FS measurements using the Wilcoxon signed-rank test ( $P > 0.05$ ). Good agreement between measurements obtained with the CS and FS acquisitions during separate breath holds was demonstrated in Bland–Altman plots of slice differences. Specifically, the mean biases of the  $R$ ,  $r$ ,  $h$ ,  $L_m$ , and SVR between the CS and FS acquisitions were 1.0%, 2.6%,  $-0.03\%$ , 1.5%, and  $-5.5\%$ , respectively. Good agreement between measurements with the CS and FS acquisitions was also observed during the single breath-hold experiments. Furthermore, there were significant differences between the morphometric parameters for the healthy and COPD subjects ( $P < 0.05$ ).

**Conclusions:** Our study has shown that HP  $^{129}\text{Xe}$  multi- $b$  diffusion MRI with CS could be beneficial in lung microstructural assessments by acquiring less data while maintaining the consistent results with the FS acquisitions. © 2018 American Association of Physicists in Medicine [https://doi.org/10.1002/mp.12944]

Key words: compressed sensing, hyperpolarized  $^{129}\text{Xe}$ , lung morphometry, multi- $b$  diffusion MRI

## 1. INTRODUCTION

Hyperpolarized (HP)  $^3\text{He}$  or  $^{129}\text{Xe}$  MRI has shown unique advantages in characterizing microstructural and functional changes in some lung diseases, such as asthma,<sup>1,2</sup> chronic obstructive pulmonary disease (COPD)<sup>3–6</sup> and radiation-induced lung injury (RILI).<sup>7–11</sup> HP gas MRI can provide quantitative and regional information about pulmonary ventilation (e.g., the ventilation defect percentage, VDP)<sup>12,13</sup> and diffusion capacity (e.g., the apparent diffusion coefficient, ADC).<sup>3,14–16</sup> Specifically, when combined with pulmonary models, such as the Weibel geometrical model<sup>17</sup> and the theoretical methods of Yablonskiy et al.,<sup>18–20</sup> HP gas multi- $b$  diffusion MRI can quantitatively probe microstructural lung parameters at the alveolar level. These parameters include acinar duct radius ( $R$ ), acinar lumen radius ( $r$ ), alveolar sleeve depth ( $h$ ), surface-to-volume ratio (SVR), and mean linear intercept ( $L_m$ ).

In previous works, multi- $b$  diffusion MRI using HP  $^3\text{He}$  was used to study lung microstructure in humans. For example, it was shown to be capable of detecting emphysematous alveolar destruction<sup>21–24</sup> and discerning changes in lung microstructure caused by different sizes of lung inflation,<sup>25</sup> different diffusion-sensitizing gradient directions<sup>26</sup> and different ages.<sup>27</sup> However, due to the long scan time required for multi- $b$  diffusion MRI, only part of the lung can be imaged in these studies. In addition, as  $^3\text{He}$  is scarce and expensive, use of HP  $^3\text{He}$  multi- $b$  diffusion MRI will be limited in future clinical applications.  $^{129}\text{Xe}$  has shorter polarization time, lower cost, and higher natural abundance than  $^3\text{He}$ , and it is therefore a potential alternative to  $^3\text{He}$ . With much smaller self-diffusion coefficients,  $^{129}\text{Xe}$  needs longer diffusion time to obtain sufficient diffusion weighting, meaning that HP  $^{129}\text{Xe}$  multi- $b$  diffusion MRI requires longer scan time than  $^3\text{He}$  MRI. In this way, it is therefore more challenging to use traditional HP  $^{129}\text{Xe}$  multi- $b$  diffusion MRI to obtain images of the whole lung in patients with limited ability to hold their breath. In previous studies that used multi- $b$  diffusion MRI with HP  $^{129}\text{Xe}$  in humans,<sup>28,29</sup> in one study a portion of the lung was covered.<sup>28</sup> In another study, MRI images with different  $b$  values were acquired over multiple breaths, which required longer scan time and larger HP gas volumes.<sup>29</sup> Therefore, there is an urgent need for new MRI methods to acquire multi- $b$  diffusion MRI data using HP  $^{129}\text{Xe}$  in a single breath hold for clinical applications.

Compressed sensing (CS) is a method for reconstructing the signal from sparse, undersampled data using special reconstruction techniques.<sup>30,31</sup> Lustig et al.<sup>32</sup> developed a framework for proton MRI using CS because  $^1\text{H}$  MRI images can be represented sparsely in a transformation domain. Thus, CS is well suited for accelerating MRI acquisitions. Ajraoui et al. demonstrated the feasibility of CS in HP  $^3\text{He}$  two-dimensional (2D) lung MRI with a two-fold acceleration factor<sup>33</sup> and with a threefold acceleration factor based on prior knowledge from  $^1\text{H}$  lung images.<sup>34</sup> The experimental results showed that the image quality of HP gas MRI with CS technique was comparable to that

with fully sampled (FS) technique. Three-dimensional (3D) acquisition using CS of both  $^3\text{He}$  images and  $^1\text{H}$  images was also achieved in one breath hold.<sup>35</sup> Moreover, some methods using CS were also studied to obtain quantitative parameters,<sup>36–39</sup> such as ADC,  $T_2^*$ , and  $B_1$  maps,<sup>36</sup> as well as velocity maps of gas airflow in the upper airway and the first bronch.<sup>37</sup> Recently, Chan et al.<sup>38</sup> tested accelerated CS acquisitions for HP  $^3\text{He}$  3D multiple  $b$  value diffusion-weighted MRI in a single breath hold and demonstrated that CS can shorten scan time. However, because there was only one COPD subject in the study, Chan et al.<sup>38</sup> did not conduct statistical analysis based on the comparison of the measurements between the healthy subjects and the COPD subject. In addition, they only reported the mean diffusion length scale ( $L_{mD}$ ) values acquired from the stretched exponential model and the ADC values. For HP gas pulmonary MRI,  $^{129}\text{Xe}$  has a more promising future in clinical applications than  $^3\text{He}$  does. It would be interesting to demonstrate the feasibility of HP  $^{129}\text{Xe}$  multi- $b$  diffusion pulmonary MRI with CS via comprehensive comparisons of different experiments and different parameters with different models. Moreover, it is important to demonstrate the effectiveness of the method in a greater number of patients with lung diseases.

In this study, we developed a method combining HP  $^{129}\text{Xe}$  multi- $b$  diffusion MRI with CS, aiming to reduce scan time and to acquire lung morphometric parameters using a cylindrical geometrical model proposed by Sukstanskii and Yablonskiy (Yablonskiy model)<sup>19</sup> during a short breath hold. Accordingly, this method can be applied to patients who are unable to hold their breath for a long time, as in cases of lung disease. To demonstrate the feasibility of our method, we employed FS and corresponding twofold accelerated undersampled CS acquisitions for the whole lung over different breath holds in five healthy subjects. We also performed the FS and synchronous CS acquisitions for one slice during a single breath hold in one healthy subject and one COPD subject. Moreover, to confirm the effectiveness of our method in clinical applications, we applied the CS acquisitions to five COPD subjects who were identified on the basis of Global Initiative for Chronic Obstructive Lung Disease criteria. Finally, we performed statistical analyses on the corresponding results obtained from the COPD and healthy subjects.

## 2. MATERIALS AND METHODS

### 2.A. Subjects

The HP  $^{129}\text{Xe}$  MRI study was conducted under the approval of the institutional review board (IRB). Prior to the HP  $^{129}\text{Xe}$  MRI experiments, all subjects signed informed consents and underwent pulmonary functions tests using a hand-held spirometer (sp-1, Schiller AG). Their blood pressure, heart rate and oxygen saturation level were monitored using a multiparameter monitor (iM8, Edan Instruments) before and after the HP  $^{129}\text{Xe}$  MRI experiments.

## 2.B. MR scanners

All imaging experiments were performed on a 1.5 T whole-body scanner (Avanto, Siemens Medical Solutions, maximum gradient strength 45 mT/m, maximum slew rate 200 mT/m/ms). A home-built transmit/receive chest coil tuned to 17.61 MHz was used for the  $^{129}\text{Xe}$  MRI experiments.

## 2.C. $^{129}\text{Xe}$ polarization

The HP  $^{129}\text{Xe}$  was polarized using a home-built polarizer based on the Rb- $^{129}\text{Xe}$  spin exchange optical pumping (Rb- $^{129}\text{Xe}$  SEOP) method.<sup>40</sup> The nuclear polarization was more than 55,000 times greater than the corresponding thermal equilibrium polarization of this gas at 1.5 T. HP xenon (86%  $^{129}\text{Xe}$ ) was cryogenically accumulated to 500-mL doses and then thawed and collected in a Tedlar bag. Five hundred milliliters of HP xenon gas and 500 mL medical-grade  $\text{N}_2$  gas were mixed into a 1 L gas mixture. After that, the gas mixture was delivered immediately to the subjects. All subjects inhaled the gas mixture at the functional residual capacity (FRC).

## 2.D. Imaging

### 2.D.1. FS acquisition

A 2D gradient echo diffusion sequence was used, and the parameters were as follows: FOV =  $384 \times 384 \text{ mm}^2$ , TR/TE = 13.9/10.9 ms, matrix =  $64 \times 64$ , number of slices = 4, slice thickness = 30 mm, slice gap = 6 mm, coronal slices, receiver bandwidth = 250 Hz/pixel, flip angle =  $5^\circ$ , and centric k-space acquisition in the phase encoding direction. The bipolar diffusion-weighted gradient pulse parameters were as follows: ramp up/down time  $\tau = 0.3$  ms, duration time  $\delta = 3.7$  ms, diffusion time  $\Delta = 5$  ms,  $b = 0, 10, 20, 30,$  and  $40 \text{ s/cm}^2$ , the diffusion gradient was applied in the slice selection direction. The total scan time was approximately 17.8 s. The parameter,  $\Delta = 5$  ms, was chosen to maximize the  $^{129}\text{Xe}$  diffusion sensitivity based on theoretical expectations,<sup>19</sup> and the five  $b$  values were chosen to decrease the fitting error.<sup>41</sup>

### 2.D.2. Retrospective CS (rCS) reconstruction

Twofold undersampling in the phase direction with a pseudo-random pattern<sup>32</sup> was used to reduce the scan time, and a random sampling scheme was used to guarantee that the undersampling artifact was incoherent in the sparse transformation domain. Reconstruction of the image involved solving the optimization problem,

$$\min_x \|F_{it}x - y\|_2^2 + \lambda_1 \|\Psi x\|_* + \lambda_2 TV(x), \quad (1)$$

where  $F_{it}$  is the transformation matrix corresponding to one of the k-space undersampled schemes,  $x$  is the reconstructed image,  $y$  is the undersampled experimental data,  $\Psi$  is the

sparse transformation matrix (here, we used Daubechie's 4 wavelet),  $TV$  is the total variation regularization, and  $\lambda_1, \lambda_2$  are weighting parameters used to balance data fidelity and artifact reduction. We used<sup>32</sup>  $\lambda_1 = 0.005$  and  $\lambda_2 = 0.002$ .

For an optimal variable-density sampled scheme, the Monte Carlo method was used to design twofold undersampled patterns. Five hundred undersampled patterns were randomly generated in the phase encoding direction. The pattern with the lowest peak interference in the transform point spread function (TPSF) was chosen to yield a high degree of incoherence. The above procedure was repeated five times to generate five different undersampled patterns, which were then simulated on the data of  $b = 0 \text{ s/cm}^2$  obtained from the FS acquisition on a healthy subject (H1) to obtain the rCS ventilation images. An optimal twofold undersampled pattern [Fig. 1(a)] was determined by minimizing the mean absolute error (MAE) between the FS and rCS ventilation images, normalizing by their respective maximum signal intensities. The MAE was the mean value of the absolute difference between the rCS and FS images over the whole lung region, pixel-by-pixel. Finally, we reconstructed images from the undersampled k-space data for all subjects.

### 2.D.3. Prospective CS acquisition

The optimal undersampled pattern in the phase encoding direction was used, resulting in a  $64 \times 32$  matrix. Therefore, the scan time was reduced from 17.8 to 8.9 s. To maintain the same consumption of magnetization in the CS acquisition as that in the FS acquisition, we raised the flip angle from  $5.0^\circ$  to  $7.0^\circ$ . In this way, up to 70% of the total  $^{129}\text{Xe}$  magnetization for imaging could be used for both acquisitions. In addition, the other parameters were the same as the corresponding parameters in the FS acquisition. The global flip angle was calibrated according to the relationship  $S(n) = S_0 \times \cos^{n-1}(\theta)$ , where  $S(n)$  is the signal after the  $n$ th pulse,  $S_0$  is the first signal of the  $^{129}\text{Xe}$ , and  $\theta$  is the flip angle.

### 2.D.4. FS and CS synchronous acquisition

To enable a direct comparison of the CS results with the FS results, the FS acquisition and the following CS acquisition, namely FS and CS synchronous acquisitions, were performed during a single breath hold. Due to the long scan time of the FS and CS synchronous acquisitions for the whole lung, only one slice was scanned. In addition, the flip angle  $3.0^\circ$  for the FS acquisition and  $4.7^\circ$  for the following CS acquisition were employed to maintain the same initial transverse magnetization and a similar consumption of magnetization for both acquisitions.

## 2.E. Image-processing and lung morphometry

The raw data were exported to the local database. Post analyses and reconstructions were performed in MATLAB (The MathWorks, Natick, MA, USA). The FS and

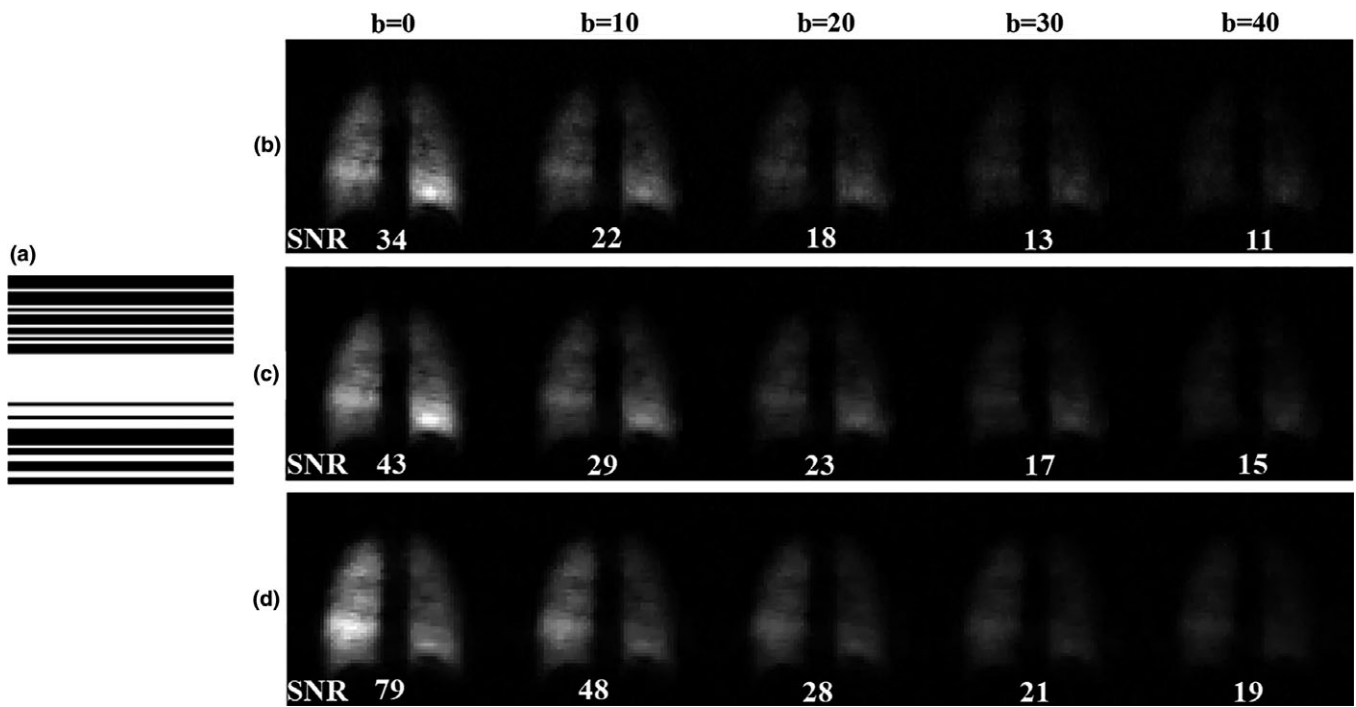


FIG. 1. (a) Optimal twofold undersampled pattern; (b) FS, (c) rCS, and (d) CS representative MR ventilation images with  $b$  values of 0, 10, 20, 30, and 40  $\text{s/cm}^2$ , and corresponding SNR values of the images in a healthy subject.

undersampled CS data were reconstructed to magnitude MRI images using the traditional 2D Fourier transform and the CS algorithm [Eq. (1)], respectively.

Because the signal-to-noise ratio (SNR) of the  $b = 0$   $\text{s/cm}^2$  image was the highest, semi-automatic segmentation (Otsu's method) was used for the  $b = 0$   $\text{s/cm}^2$  image to segment the lung mask, excluding background noise and unventilated lung regions. Large conducting airways were also removed. Then, the resulting mask was applied to all other corresponding images.

All maps of morphometric parameters were produced based on the mathematical model [equation (2–5) and (10–13) in the Ref. 19] of  $^{129}\text{Xe}$  diffusion in human lungs as proposed by Sukstanskii and Yablonskiy. To reduce the effect of the flip angle, the  $S(b)/(S_0 \cos^2 \theta)$  was fitted as a function of  $b$  value using a nonlinear least squares algorithm on a pixel-by-pixel basis, where  $S(b)$  and  $S_0$  are the magnitudes of the corresponding images with  $b \neq 0$  and  $b = 0$   $\text{s/cm}^2$ , and  $n = 1, 2, 3, 4$  for  $b = 10, 20, 30, 40$   $\text{s/cm}^2$ , respectively. Accordingly, the best-fit  $r$  and  $R$  were directly obtained. Then, the other parameters, such as  $h$ ,  $L_m$ , and SVR, were obtained via the relevant equations.<sup>19</sup> The maps and the mean values of the morphometric parameters and ADC (generated from  $b = 0, 10$   $\text{s/cm}^2$  mono-exponential fitting) were calculated, and then these results were compared among the CS, rCS and FS measurements for each subject.

## 2.F. Data analysis

The Wilcoxon signed-rank test was employed to measure the significance of the differences between the rCS and FS

results, pixel-by-pixel. Because the FS and CS images of the whole lung from the healthy subjects were acquired in different breath-hold scans, we only compared the mean values of the morphometric parameters of the corresponding slices and the globe lung. To confirm agreement between measurements obtained from the FS and CS acquisitions, for the FS and CS acquisitions during separate breath holds, the Bland–Altman plots by a comparison of the relative differences in the mean values at the slice-by-slice level were constructed, and the relative differences in global mean values were also calculated. For the FS and CS synchronous acquisitions during a single breath hold, the structural similarity (SSIM) index of the FS and CS images and the differences in the mean morphometric parameter values between the FS and CS acquisitions were calculated. For statistical analyses of the morphometric parameters between the healthy and COPD subjects, the two-tailed  $t$ -test (two-sample comparison of mean) was performed, according to the equivalence of the variances demonstrated by the  $F$ -test. In all statistical analyses, a  $P < 0.05$  was considered statistically significant.

## 3. RESULTS

### 3.A. Subjects

All the subjects, six healthy subjects (mean age, 26 years  $\pm$  3; range, 23–30 years) and six COPD subjects (mean age, 58 years  $\pm$  5; range, 53–65 years), could tolerate  $^{129}\text{Xe}$  inhalations and breath holds. No adverse events were detected during the lung MRI, and no significant changes were found in terms of blood pressure, heart rate or oxygen

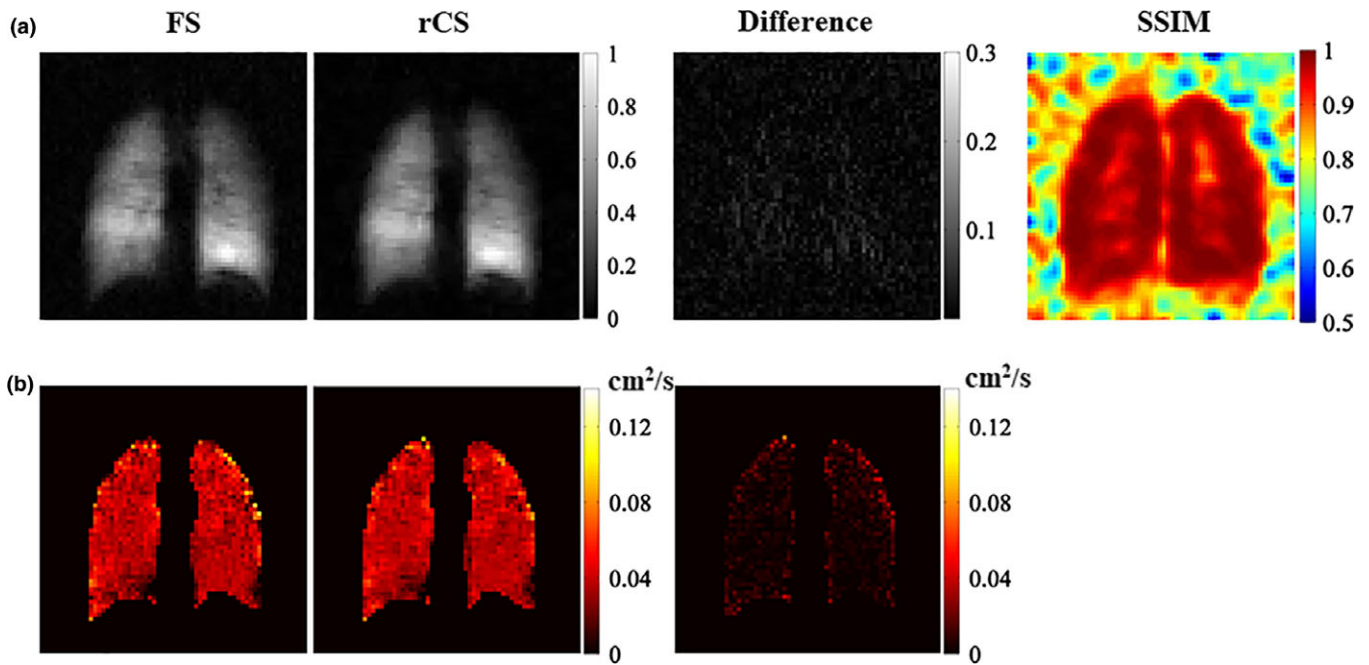


FIG. 2. (a) FS and rCS ventilation images with  $b$  value of 0 and their corresponding difference map and SSIM map; (b) ADC maps obtained from FS and rCS acquisitions and their corresponding difference ADC map. [Color figure can be viewed at [wileyonlinelibrary.com](http://wileyonlinelibrary.com)]

saturation levels in any of the subjects after HP  $^{129}\text{Xe}$  experiments.

### 3.B. FS and CS acquisitions during separate breath holds

The representative multi- $b$  diffusion MR images obtained with the FS, rCS, and CS acquisitions for a healthy subject (H1) are shown in Figs. 1(b)–1(d). A decrease in signal intensity with an increasing  $b$  value was observed, corresponding to the increased signal dephasing induced by larger diffusion gradients. There were no evident visual differences among the FS, rCS, and CS images, except that the rCS and CS images were smoother than the FS images, as was expected due to the nature of the CS reconstruction.<sup>33</sup> The corresponding SNR values of the FS, rCS, and CS images were successively increased. The corresponding MAE computed over the lung region between the FS and rCS images were 0.008, 0.012, 0.013, 0.015, and 0.016 for the diffusion-weighted images with  $b$  values of 0, 10, 20, 30, and 40 s/cm<sup>2</sup>, respectively. The MAE increased as the SNR decreased.

Figure 2(a) shows the FS and rCS images of  $b = 0$  s/cm<sup>2</sup>, the corresponding difference map and the SSIM map for a representative slice (as shown in Fig. 1). No obvious difference was found between the FS and rCS images. The mean SSIM values in the lung field of the representative slice and the whole lung were 0.974 and 0.971, respectively. The SSIM map and the mean SSIM values indicated that the detail and the edge of the images were well-preserved in the CS reconstruction. Figure 2(b) shows the ADC maps obtained from the FS and rCS acquisitions and the corresponding difference ADC map. Large differences in the edge of the lung were

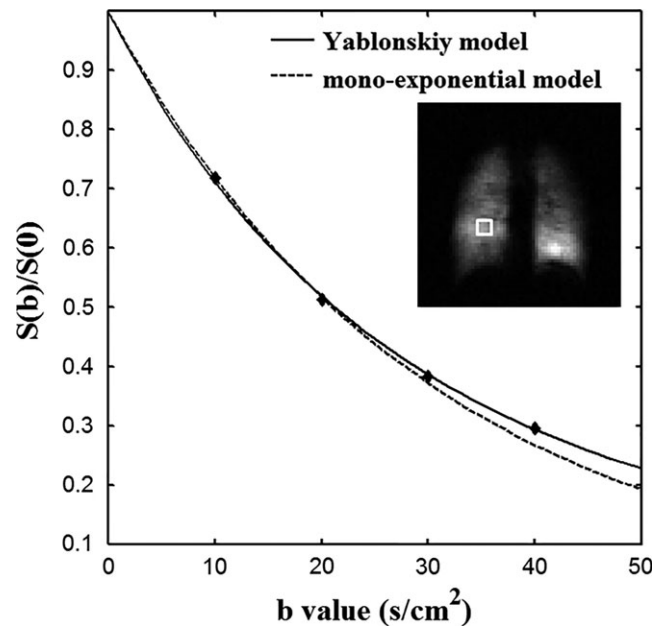


FIG. 3. Fitting curves with the mono-exponential model and Yablonskiy model, using the mean values of the pulmonary parenchyma measured from a region of interest in a healthy subject lung. The solid line is a fit to the Yablonskiy model, and the dashed line is a fit to a mono-exponential model.

found in the difference ADC map. These differences may be attributable to the low SNR.

Figure 3 shows the fitting curves with the mono-exponential model using the first two data points ( $b = 0$  and  $b = 10$  s/cm<sup>2</sup>) and Yablonskiy model. The points obviously deviated from the mono-exponential curve due to the non-Gaussian nature of the xenon diffusion in the lungs.

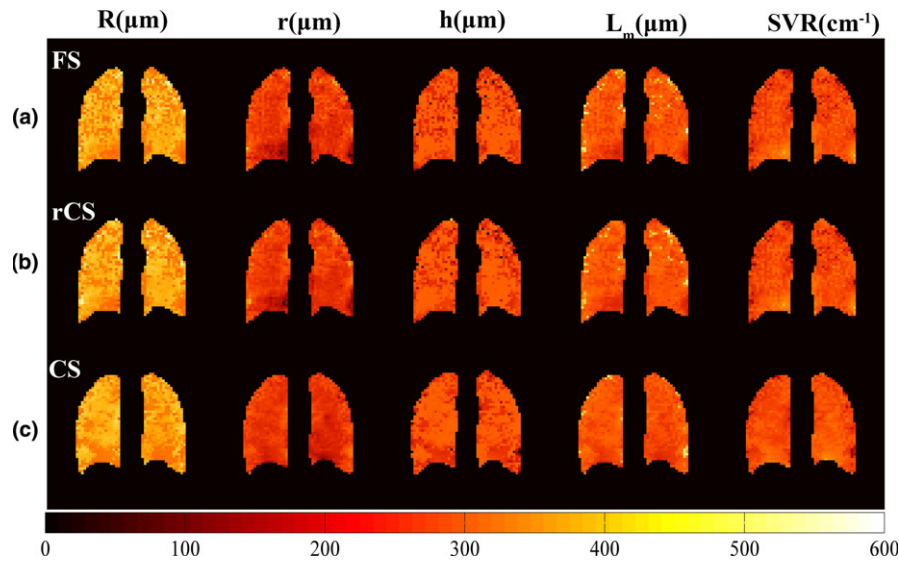


FIG. 4. Representative maps of the morphometric parameters from (a) FS, (b) rCS, and (c) CS acquisitions for a healthy subject. [Color figure can be viewed at wileyonlinelibrary.com]

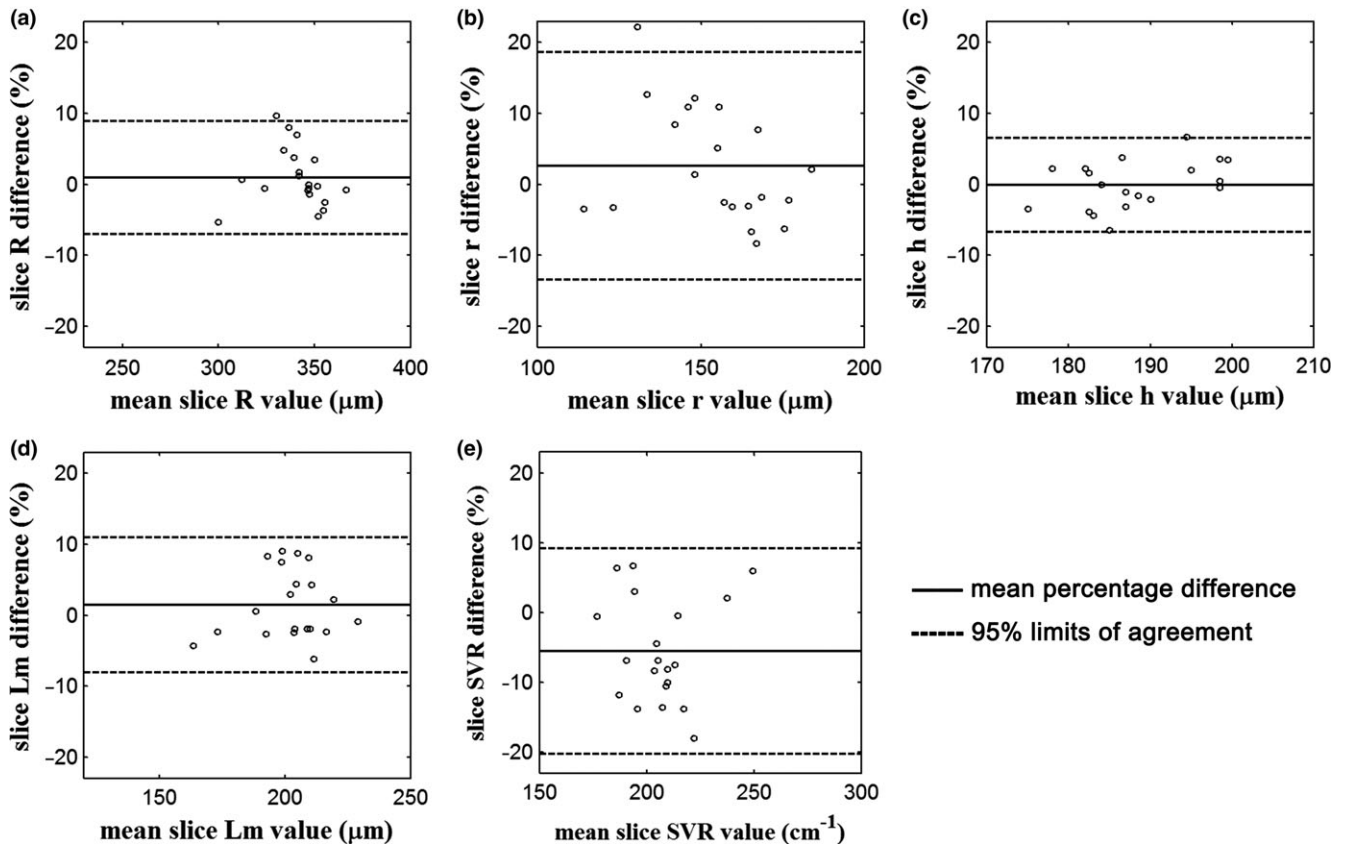


FIG. 5. Bland–Altman plots of mean slice (a) R, (b) r, (c) h, (d)  $L_m$ , and (e) SVR values from FS and CS acquisitions. The solid lines represent the mean percentage differences, and the dash lines represent the 95% limits of agreement.

Yablonskiy model could accurately describe the non-Gaussian diffusion of xenon gas in the pulmonary parenchyma.

Figure 4 shows the maps of the morphometric parameters derived from calculating the FS, rCS, and CS MRI dataset from the representative slice (as shown in Fig. 1). These maps were homogeneous, as observed in other studies.<sup>29,38</sup> In

Figs. 4(a) and 4(b), the p-values of the Wilcoxon signed-rank test for the morphometric parameters were all greater than 0.05, indicating that there were no significant differences between the FS and rCS measurements. In Figs. 4(a) and 4(c), there were some slight differences in the lung sizes and positions. The main reason for these differences may be that

TABLE I. Lung morphometric parameters and differences between measurements from different acquisitions.

Parameters	Method	Healthy					Mean ± SD
		H1	H2	H3	H4	H5	
SNR	FS	33 ± 8	26 ± 5	43 ± 4	35 ± 9	27 ± 3	33 ± 6
	rCS	46 ± 18	31 ± 6	56 ± 5	48 ± 17	34 ± 4	43 ± 9
	CS	97 ± 9	88 ± 6	80 ± 5	79 ± 17	59 ± 4	81 ± 14
Diff. (%)		<b>184</b>	<b>238</b>	<b>86</b>	<b>125</b>	<b>118</b>	<b>150 ± 61</b>
ADC (cm <sup>2</sup> /s)	FS	0.0398 ± 0.0121	0.0356 ± 0.0128	0.0349 ± 0.0118	0.0415 ± 0.0146	0.0323 ± 0.0133	0.0370 ± 0.0033
	rCS	0.0397 ± 0.0115	0.0353 ± 0.0114	0.0350 ± 0.0118	0.0414 ± 0.0135	0.0322 ± 0.0126	0.0368 ± 0.0030
	CS	0.0385 ± 0.0084	0.0367 ± 0.0084	0.0376 ± 0.0072	0.0394 ± 0.0113	0.0307 ± 0.0081	0.0364 ± 0.0030
<i>P</i> value		<b>0.098</b>	<b>0.154</b>	<b>0.245</b>	<b>0.193</b>	<b>0.438</b>	
Diff. (%)		<b>-3.3</b>	<b>3.0</b>	<b>7.7</b>	<b>-5.0</b>	<b>-4.7</b>	<b>-0.5 ± 5.0</b>
R (μm)	FS	354 ± 62	329 ± 59	327 ± 52	363 ± 70	324 ± 63	339 ± 15
	rCS	356 ± 60	330 ± 57	327 ± 54	364 ± 67	325 ± 62	340 ± 15
	CS	352 ± 70	349 ± 63	345 ± 66	351 ± 70	314 ± 67	342 ± 13
<i>P</i> value		<b>0.074</b>	<b>0.064</b>	<b>0.345</b>	<b>0.076</b>	<b>0.418</b>	
Diff. (%)		<b>-0.6</b>	<b>6.1</b>	<b>5.5</b>	<b>-3.3</b>	<b>-3.1</b>	<b>0.9 ± 4.1</b>
r (μm)	FS	170 ± 45	143 ± 41	135 ± 32	175 ± 40	133 ± 46	151 ± 16
	rCS	171 ± 44	144 ± 35	135 ± 33	176 ± 35	134 ± 44	152 ± 16
	CS	173 ± 42	158 ± 36	152 ± 39	170 ± 44	134 ± 40	157 ± 13
<i>P</i> value		<b>0.064</b>	<b>0.056</b>	<b>0.051</b>	<b>0.145</b>	<b>0.116</b>	
Diff. (%)		<b>1.8</b>	<b>10.5</b>	<b>12.6</b>	<b>-2.9</b>	<b>0.8</b>	<b>4.6 ± 5.9</b>
h (μm)	FS	198 ± 43	189 ± 48	195 ± 41	187 ± 58	194 ± 47	193 ± 4
	rCS	196 ± 45	189 ± 46	195 ± 40	188 ± 56	196 ± 50	193 ± 4
	CS	194 ± 42	193 ± 45	190 ± 42	187 ± 49	186 ± 38	190 ± 3
<i>P</i> value		<b>0.348</b>	<b>0.087</b>	<b>0.182</b>	<b>0.184</b>	<b>0.054</b>	
Diff. (%)		<b>-2.0</b>	<b>2.1</b>	<b>-2.6</b>	<b>0.0</b>	<b>-4.1</b>	<b>-1.3 ± 2.1</b>
L <sub>m</sub> (μm)	FS	213 ± 38	189 ± 37	201 ± 45	219 ± 37	184 ± 39	201 ± 12
	rCS	214 ± 37	190 ± 35	201 ± 44	220 ± 35	184 ± 38	202 ± 12
	CS	209 ± 37	205 ± 37	214 ± 40	214 ± 45	173 ± 35	203 ± 14
<i>P</i> value		<b>0.067</b>	<b>0.120</b>	<b>0.608</b>	<b>0.227</b>	<b>0.501</b>	
Diff. (%)		<b>-1.9</b>	<b>8.5</b>	<b>6.5</b>	<b>-2.3</b>	<b>-6.0</b>	<b>1.0 ± 5.5</b>
SVR (cm <sup>-1</sup> )	FS	189 ± 40	216 ± 43	225 ± 38	184 ± 37	225 ± 46	208 ± 16
	rCS	188 ± 39	215 ± 38	224 ± 38	183 ± 35	224 ± 45	207 ± 16
	CS	193 ± 39	200 ± 39	195 ± 31	192 ± 44	228 ± 46	202 ± 12
<i>P</i> value		<b>0.058</b>	<b>0.074</b>	<b>0.080</b>	<b>0.207</b>	<b>0.102</b>	
Diff. (%)		<b>2.1</b>	<b>-7.4</b>	<b>-13.3</b>	<b>4.3</b>	<b>1.3</b>	<b>-2.6 ± 6.6</b>

SNR and morphometric parameter values represent mean ± standard deviations (SD) of the whole lung; Diff. represents percentage of relative difference between CS and FS measurements; *P* value represents difference between rCS and FS measurements on a pixel-by-pixel basis using a Wilcoxon signed-rank test. The bold values represent the results of statistical analyses between FS and rCS/CS.

the FS and CS acquisitions were obtained during different breath holds.

The Bland–Altman analyses of the mean morphometric parameters on the slice-by-slice basis between the FS and CS acquisitions are shown in Fig. 5. The mean biases of the R, r, h, L<sub>m</sub>, and SVR values between the CS and FS acquisitions were 1.0%, 2.6%, -0.03%, 1.5%, and -5.5%, respectively. Good agreements between the measurements obtained with the CS and FS acquisitions were observed in the Bland–Altman plots.

Table I provides the global mean values of the morphometric parameters, SNR and ADC from the FS, rCS, and CS acquisitions for five healthy subjects. Table I also provides the *P* values of the Wilcoxon signed-rank test between FS

and rCS measurements and the relative differences in the global mean values between CS and FS measurements. The *P* values were all greater than 0.05, indicating that there were no significant differences between the FS and rCS acquisitions (at the significance level of 0.05). The relative differences in the global mean values of morphometric parameters and ADC between the FS and CS acquisitions were within their respective standard deviation ranges.

### 3.C. FS and CS synchronous acquisitions during a single breath hold

Figure 6 shows the FS and CS images of *b* = 0 s/cm<sup>2</sup>, the corresponding difference and SSIM maps during a single

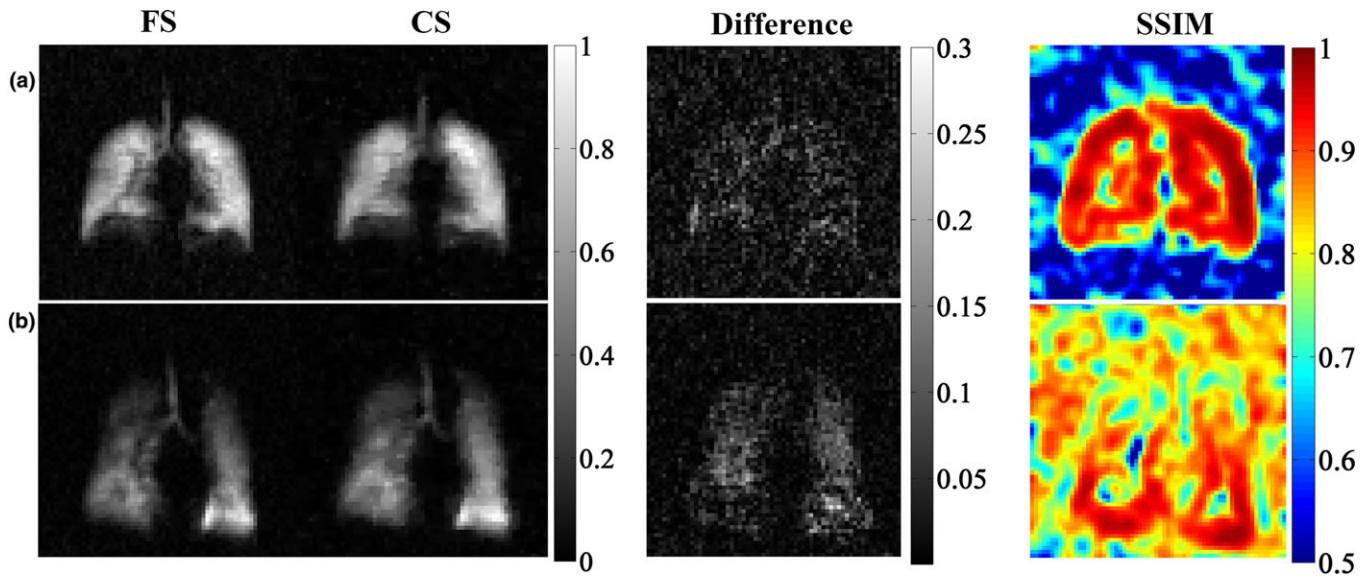


FIG. 6. FS and CS images of  $b = 0 \text{ s/cm}^2$ , corresponding difference maps, and SSIM maps during a single breath hold from (a) a healthy subject and (b) a COPD patient. [Color figure can be viewed at [wileyonlinelibrary.com](http://wileyonlinelibrary.com)]

breath hold for a healthy subject (H6) and a COPD subject (C6). For both sets of data, the images with good quality were obtained. The CS images were smoother than the corresponding FS images. The MAE and the mean SSIM values in the lung region were 0.0107 and 0.913 for the healthy subject, respectively, and 0.0163 and 0.877 for the COPD subject, respectively. The difference between the FS and CS images was larger in the COPD subject than in the healthy subject.

The maps and the mean values of the morphometric parameters of the slices (as shown in Fig. 6) are presented in Fig. 7 and Table II, respectively. There are some differences between the mean values of the morphometric parameters of the FS and CS acquisitions, although they were determined from images acquired during a single breath hold. This demonstrates that the differences derive not from the lung size but rather from the CS acquisition and reconstruction. The maps of the morphometric parameters from the COPD subject were heterogeneous, and the mean  $R$ ,  $r$ , and  $L_m$  values were larger while the mean  $h$  and  $SVR$  values were lower than those from the healthy subject. These results indicate that airspace enlargement and heterogeneous increase exist in the lung of the COPD subject.

### 3.D. Comparisons of measurements between the healthy and COPD subjects

Table III presents the pulmonary function measurements and the global mean values of the morphometric parameters for five healthy subjects and five COPD subjects. The mean values of the morphometric parameters from the healthy subjects were adjusted for aging effects based on the results from previous studies.<sup>27</sup> On average, the COPD subjects were 32 years older than the healthy subjects. Therefore, according to the previously established relationships,<sup>27</sup> the age-adjusted mean values for the healthy subjects were as follows,

$$R_a = (0.45 \pm 0.2) \times \Delta \text{age} + R_0 \quad (2)$$

$$r_a = (1.3 \pm 0.3) \times \Delta \text{age} + r_0 \quad (3)$$

$$h_a = (-0.87 \pm 0.2) \times \Delta \text{age} + h_0 \quad (4)$$

$$L_{m,a} = (1.4 \pm 0.4) \times \Delta \text{age} + L_{m,0} \quad (5)$$

$$SVR_a = (-1.1 \pm 0.3) \times \Delta \text{age} + SVR_0 \quad (6)$$

where  $R_a$ ,  $r_a$ ,  $h_a$ ,  $L_{m,a}$ , and  $SVR_a$  are the age-adjusted mean values,  $R_0$ ,  $r_0$ ,  $h_0$ ,  $L_{m,0}$ , and  $SVR_0$  are the original mean values (as the CS results shown in Table I), and  $\Delta \text{age}$  (i.e., 32 years old) is the difference in the ages between the age-adjusted and original data. The  $P$  values of the  $t$ -test between the morphometric parameters from the healthy and COPD subjects were all less than 0.05, indicating that all the morphometric parameters from the COPD group exhibited significant differences in comparison with those from the healthy group.

## 4. DISCUSSION

In this study, we developed an accelerated HP  $^{129}\text{Xe}$  multi- $b$  diffusion MRI with CS method and demonstrated its utility in identifying the alterations of the lung microstructures in patients with COPD as compared to the healthy subjects. The results indicate that this method is able to greatly reduce the scan time from 17.8 to 8.9 s, and the lung morphometric parameters obtained with the CS acquisition are in agreement with those obtained with the FS acquisition. The morphometric parameters from the COPD subjects were significantly different from those from the healthy subjects. These findings were consistent with the results from previous related studies.<sup>23,29</sup>

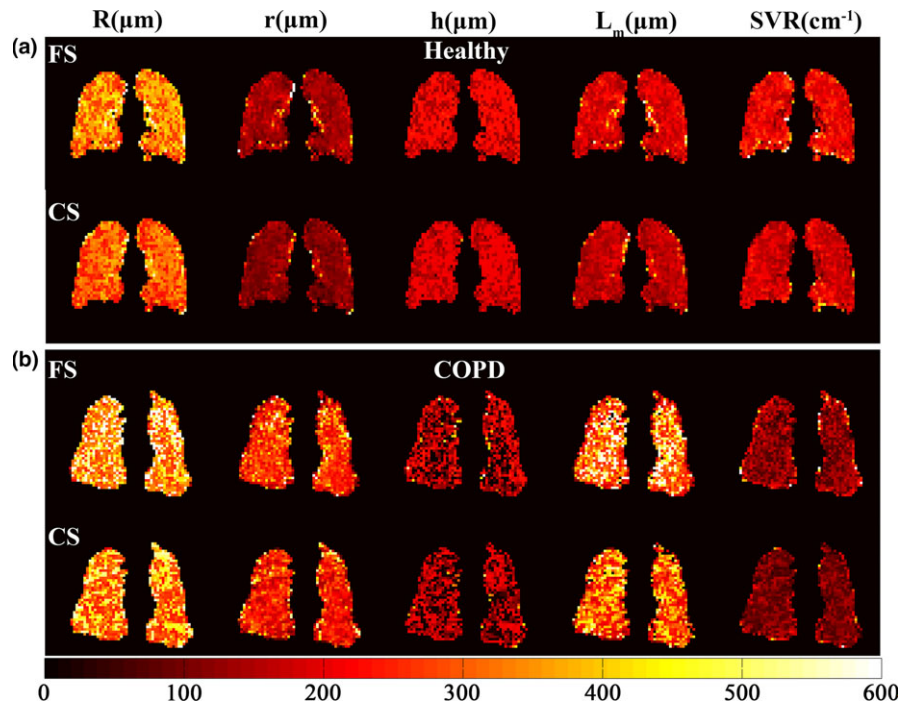


FIG. 7. Morphometric parameter maps obtained from FS and CS synchronous acquisitions during a single breath hold for (a) a healthy subject and (b) a COPD subject. [Color figure can be viewed at [wileyonlinelibrary.com](http://wileyonlinelibrary.com)]

TABLE II. Morphometric parameters from a healthy subject (H6) and a COPD subject (C6).

Subjects	Age(years)	Method	ADC ( $\text{cm}^2/\text{s}$ )	R ( $\mu\text{m}$ )	r ( $\mu\text{m}$ )	h ( $\mu\text{m}$ )	$L_m$ ( $\mu\text{m}$ )	SVR ( $\text{cm}^{-1}$ )
H6	28	FS	$0.0355 \pm 0.0130$	$346 \pm 82$	$150 \pm 68$	$195 \pm 48$	$198 \pm 65$	$218 \pm 83$
		CS	$0.0348 \pm 0.0106$	$353 \pm 73$	$143 \pm 60$	$211 \pm 46$	$199 \pm 58$	$214 \pm 54$
		Diff. (%)	<b>-2.0</b>	<b>2.0</b>	<b>-4.7</b>	<b>8.2</b>	<b>0.5</b>	<b>-1.8</b>
C6	60	FS	$0.0572 \pm 0.0223$	$395 \pm 122$	$261 \pm 99$	$135 \pm 73$	$357 \pm 155$	$139 \pm 79$
		CS	$0.0561 \pm 0.0184$	$420 \pm 123$	$277 \pm 102$	$144 \pm 97$	$355 \pm 122$	$137 \pm 60$
		Diff. (%)	<b>-1.9</b>	<b>6.3</b>	<b>6.1</b>	<b>6.7</b>	<b>-0.6</b>	<b>-1.4</b>

Morphometric parameter values represent mean  $\pm$  standard deviations for one slice; Diff. represents percentage of relative difference between CS and FS measurements. The bold values represent the differences between FS and CS measurement, and they were mentioned in the discussion part. Therefore, they need to be highlighted.

Due to the low SNR of MR images and the long acquisition time of HP  $^{129}\text{Xe}$  multi-*b* diffusion MRI, a low spatial resolution ( $6 \text{ mm} \times 6 \text{ mm}$ ) was used in this study. However, because we mainly focused on the lung morphometric parameters, the low spatial resolution still meets the theoretical<sup>19</sup> and experimental requirements.<sup>23,25–28</sup> In addition, the centric k-space acquisition in the phase encoding direction was used to optimize the SNR. The ventilation images were, therefore, somewhat blurred. Also, the SNR of the FS, rCS and CS ventilation images increased gradually, possibly due to two main reasons. One reason could be the denoising properties inherent to CS.<sup>32</sup> In the CS reconstruction, the pre-knowledge of sparsity, such as the piecewise smooth assumption, could result in a higher apparent SNR because the background noise is heavily suppressed. The other reason could be the larger flip angle in the prospective CS acquisition. The larger flip angle could also have resulted in a higher SNR because of increased signal strength.

In this study, the mean R and r values from the healthy subjects ( $342 \mu\text{m}$  and  $157 \mu\text{m}$ ) were slightly higher than those from previous studies (approximately  $310 \mu\text{m}$  and  $140 \mu\text{m}$ ) using HP  $^3\text{He}$  multi-*b* diffusion MRI.<sup>26,27</sup> These differences may be attributable to several factors. First, the SNR of the HP  $^{129}\text{Xe}$  MR image is generally lower than that of the HP  $^3\text{He}$  MR image, and the lower SNR could lead to higher deviations from the true values in the morphometric measurements. Moreover, the gradient strength could also have an impact on the results, possibly producing approximately 15% and 3% relative error for R and r for the maximum 35.3 mT/m used in our study.<sup>19</sup> The different fitting models for  $^{129}\text{Xe}$  and  $^3\text{He}$  may have played a role in the results as well.<sup>18,19</sup> For the other morphometric values, the mean  $L_m$  ( $203 \mu\text{m}$ ) and SVR ( $202 \text{ cm}^{-1}$ ) values were in agreement with those from previous studies (approximately  $200 \mu\text{m}$  and  $200 \text{ cm}^{-1}$  for  $L_m$  and SVR, respectively).<sup>26,27</sup> However, the h value ( $190 \mu\text{m}$ ) was larger than that (approximately  $140 \mu\text{m}$ ) from

TABLE III. PFT measurements and morphometric parameters for five healthy subjects (H1–H5) and five COPD subjects (C1–C5).

Subjects	Age (years)	FEV <sub>1</sub> /FVC (%)	%FEV <sub>1</sub> (%)	ADC (cm <sup>2</sup> /s)	R (μm)	r (μm)	h (μm)	L <sub>m</sub> (μm)	SVR (cm <sup>-1</sup> )
H1	26	79	106	0.0385 ± 0.0084	366 ± 6	212 ± 10	170 ± 6	254 ± 13	154 ± 10
H2	30	79	93	0.0367 ± 0.0084	363 ± 6	185 ± 10	161 ± 6	250 ± 13	181 ± 10
H3	26	82	110	0.0376 ± 0.0072	359 ± 6	177 ± 10	167 ± 6	260 ± 13	190 ± 10
H4	24	85	105	0.0394 ± 0.0113	365 ± 6	217 ± 10	159 ± 6	260 ± 13	149 ± 10
H5	23	83	100	0.0307 ± 0.0081	328 ± 6	175 ± 10	166 ± 6	217 ± 13	190 ± 10
Mean ± SD	<b>26 ± 3</b>	<b>82 ± 3</b>	<b>103 ± 7</b>	<b>0.0364 ± 0.0030</b>	<b>356 ± 14</b>	<b>193 ± 18</b>	<b>165 ± 4</b>	<b>248 ± 16</b>	<b>173 ± 18</b>
C1	62	64	70	0.0546 ± 0.0158	414 ± 90	288 ± 41	126 ± 47	394 ± 119	109 ± 29
C2	53	56	68	0.0506 ± 0.0175	391 ± 94	261 ± 45	129 ± 52	373 ± 122	122 ± 35
C3	65	68	112	0.0603 ± 0.0123	374 ± 82	242 ± 50	138 ± 50	304 ± 85	135 ± 39
C4	56	64	105	0.0434 ± 0.0089	361 ± 83	213 ± 47	148 ± 54	286 ± 99	155 ± 43
C5	53	67	89	0.0430 ± 0.0097	381 ± 78	207 ± 46	174 ± 45	275 ± 79	156 ± 34
Mean ± SD	<b>58 ± 5</b>	<b>64 ± 5</b>	<b>89 ± 18</b>	<b>0.0504 ± 0.0067</b>	<b>386 ± 18</b>	<b>242 ± 30</b>	<b>143 ± 17</b>	<b>326 ± 47</b>	<b>135 ± 18</b>
<i>P</i> -value	<b>&lt;0.001</b>	<b>&lt;0.001</b>	<b>0.174</b>	<b>0.005</b>	<b>0.032</b>	<b>0.022</b>	<b>0.040</b>	<b>0.014</b>	<b>0.019</b>

Morphometric parameter values represent mean ± standard deviations for the whole lung; Morphometric parameter values for healthy subjects are from CS acquisitions and age-adjusted; *P* value represents difference between COPD and healthy subjects using a two-sample *t*-test. The bold values represent the results of statistical analyses of two sets of data for healthy and COPD groups.

previous studies.<sup>26,27</sup> Compared to the studies of HP gas multi- $b$  diffusion MRI using  $^3\text{He}$  in humans, the studies using  $^{129}\text{Xe}$  are scarce. The small differences between our results and the others might be attributed to the different fitting methods<sup>29</sup> or to the different  $B_0$  field strengths.<sup>28</sup> Overall, our results were consistent with those from the previous studies,<sup>26–29</sup> but were not exactly the same.

The CS and FS measurements showed limited variations during separate breath holds. The mean values of the differences in the global R, r, h, L<sub>m</sub>, and SVR values were 0.9%, 4.6%, -1.3%, 1.0%, and -2.6%, respectively. There are several possible reasons. First, the FS and CS acquisitions were completed during different breath holds. Although the subjects were instructed to inhale the same  $^{129}\text{Xe}$  and N<sub>2</sub> gas dosage during each acquisition, the lung inflation volume could not be absolutely identical across different breath holds due to moderate movement or variation in ventilation.<sup>6,35</sup> Therefore, the morphometric parameters may have been affected slightly.<sup>25</sup> Second, the SNR of the FS and CS images were different. The SNR of the CS image was generally higher than that of the corresponding FS image. The SNR could affect the anisotropic diffusion coefficient estimations and, consequently, the morphometric parameters.<sup>21,41</sup> Moreover, the CS reconstruction algorithms could contribute to the differences as well.<sup>38</sup> The direct comparisons of the CS and FS measurements during a single breath hold indicate that the differences may mainly be attributable to the CS reconstruction. Additionally, the differences between the CS and FS measurements during a single breath hold were larger for the COPD subject than for the healthy subject. One possible explanation for this could be that there was delayed ventilation in the poorly ventilated region of the COPD subject.<sup>42</sup> Another possible explanation could be that the signal distribution of the image was heterogeneous for the COPD subject and homogenous for the healthy subject. The smoothing effect of the CS reconstruction has greater influence on heterogeneous signal distributions. Moreover, the

undersampled pattern was obtained from a healthy subject and may not fit well for the COPD subject due to the different signal distribution.

Although small differences were observed between the morphometric parameters derived from the CS acquisitions and those derived from the FS acquisitions, these differences were within their respective standard deviation ranges and are negligible compared to the heterogeneity across the whole lung.<sup>17</sup> Compared to the mean values of the morphometric parameters from the healthy subjects, the mean values of R, r, h, L<sub>m</sub>, and SVR from the COPD subjects increased by 12.7%, 54.1%, -24.7%, 60.6%, and -33.2%, respectively. Even for the age-adjusted morphometric parameter values, these mean values increased by 8.4%, 25.4%, -13.3%, 31.5%, and -22.0%, respectively. Therefore, differences in the morphometric parameters between the FS and CS acquisitions may be of lesser importance than differences between the healthy and COPD subjects.

The mean values of R, r, and L<sub>m</sub> were higher in the COPD subjects, while h and SVR were lower than in the healthy subjects. This indicates that the lung airspaces enlarge in the COPD subjects. These results were consistent with those from previous studies.<sup>23,29</sup> Results of the statistical analysis show that the morphometric parameters from the COPD subjects differ significantly from those from the healthy subjects. This difference exists even for the age-adjusted parameters from the healthy subjects, which further proves that the two groups can be easily differentiated. These results show that  $^{129}\text{Xe}$  multi- $b$  diffusion MRI with CS is sensitive to the changes in lung microstructure. Therefore, it could effectively detect lung diseases associated with emphysema.

Parallel imaging (PI) with multiple receive channels is another acceleration method that can be used to reduce scan time in MRI. The lung morphometry was measured with accelerated hyperpolarized  $^3\text{He}$  diffusion MRI with an 8-channel receive coil and the parallel imaging method.<sup>43</sup> However, this method requires an additional array of RF channels

and coils. In addition, partial-Fourier sampling method can also reduce the scan time. As demonstrated in previous studies,<sup>33,36</sup> the image quality produced by this method is poorer than that of the CS reconstruction image, while time reduction remains the same.

In our method, the scan time of a single coronal slice was approximately 2.2 s. Therefore, the method could afford the possibility of covering the entire lung volume in 8.8 to 15.4 s (~4–7 slices, 138–246 mm) for most subjects. Furthermore, with a combination of CS and PI techniques in the future, the scan time could be reduced further, and the image resolution could also be improved. In addition, the method could also be combined with other models such as the  $q$ -space,<sup>44,45</sup> stretched exponential,<sup>46</sup> and diffusion kurtosis imaging (DKI)<sup>47,48</sup> models to probe lung microstructure. Hence, HP  $^{129}\text{Xe}$  multi- $b$  diffusion MRI with CS has great potential for clinical applications, and it could be applied perfectly well in subjects with lung diseases who may be unable to hold their breath for a long time.

Some limitations exist in this study. First, a limited number of subjects were recruited. Only six healthy subjects and six COPD patients were recruited for the study. This number of subjects is, however, sufficient to demonstrate the feasibility and effectiveness of this method in the present study and under the existing circumstances. Second, the ages of the COPD and the healthy groups were not well matched. In our study, all the subjects in the healthy group were younger than those in the COPD group. Only young people were recruited as healthy subjects because it is much easier for them to tolerate the long breath holds (approximately 18 s for FS acquisition), which might pose challenges for elderly people. However, we adjusted our results for age-related changes in lung microstructure<sup>27</sup> to minimize the age effect. In the future, we might conduct more studies with age-matched groups (the healthy subjects and the patients of different lung diseases) to confirm the effectiveness of the method. Third, due to the limited sparsity and phase encoding steps in the 2D CS HP gas imaging, the large acceleration factor could not be used to maintain the high image quality. Therefore, we only used an acceleration factor of 2 for this study. The 3D CS HP gas imaging method can use a larger acceleration factor and still maintain a moderately high image quality.<sup>33,35,38</sup> Hence, a 3D acquisition with CS will be developed in the future. Fourth, the undersampled pattern was obtained from only one healthy subject. It may not fit the COPD subjects very well due to the heterogeneity of the signal distribution. In the future, we will further optimize the undersampled pattern using a larger database that features a greater number of diseased subjects.

## 5. CONCLUSIONS

By using compressed sensing, we are able to make a 2D acquisition of HP  $^{129}\text{Xe}$  multi- $b$  diffusion MRI in a single breath hold. This new method allows us to identify changes in the lung morphology of COPD subjects as compared to healthy subjects.

## ACKNOWLEDGMENTS

We acknowledge the support by the National Key R&D Program of China (2016YFC1304700 and 2017YFA0505400), the National Natural Science Foundation of China (81227902, 81625011), the Key Research Program of Frontier Sciences (QYZDY-SSW-SLH018) and the Strategic Priority Research (XDB21010200), CAS. XZ acknowledges the support by the National Program for Support of Eminent Professionals (National Program for Support of Top-notch Young Professionals). We thank Professor Louis S. Bouchard for editing our manuscript.

## CONFLICT OF INTEREST

The authors have no conflict of interest to disclose.

<sup>a)</sup>Author to whom correspondence should be addressed. Electronic mail: xinzhou@wipm.ac.cn

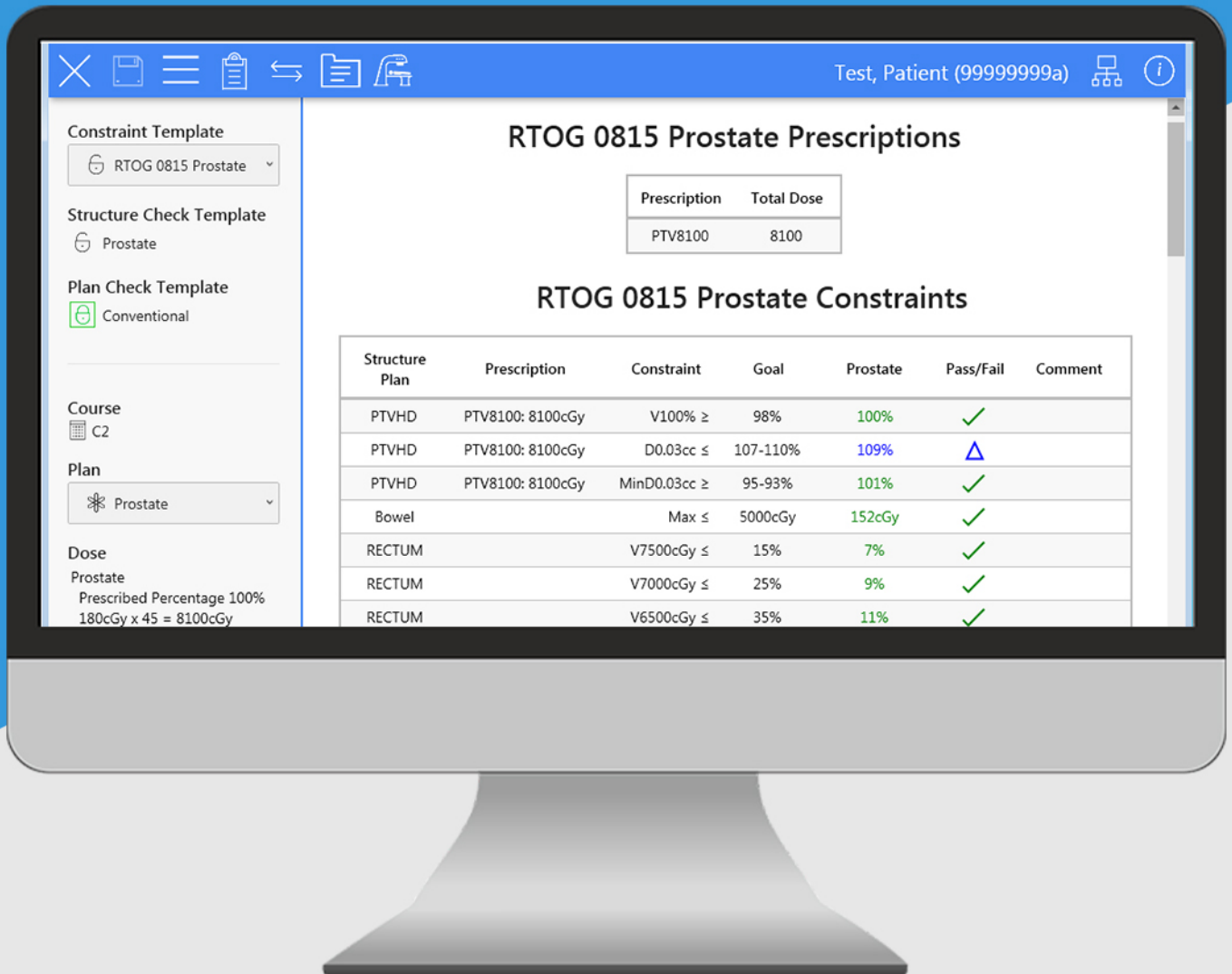
## REFERENCES

1. Thomen RP, Sheshadri A, Quirk JD, et al. Regional ventilation changes in severe asthma after bronchial thermoplasty with  $^3\text{He}$  MR imaging and CT. *Radiology*. 2015;274:250–259.
2. Cadman RV, Lemanske RF Jr, Evans MD, et al. Pulmonary  $^3\text{He}$  magnetic resonance imaging of childhood asthma. *J Allergy Clin Immunol*. 2013;131:369–376.
3. Kaushik SS, Cleveland ZI, Cofer GP, et al. Diffusion-weighted hyperpolarized  $^{129}\text{Xe}$  MRI in healthy volunteers and subjects with chronic obstructive pulmonary disease. *Magn Reson Med*. 2011;65:1154–1165.
4. Wang C, Altes TA, Mugler JP 3rd, et al. Assessment of the lung microstructure in patients with asthma using hyperpolarized  $^3\text{He}$  diffusion MRI at two time scales: comparison with healthy subjects and patients with COPD. *J Magn Reson Imaging*. 2008;28:80–88.
5. Qing K, Mugler JP III, Altes TA, et al. Assessment of lung function in asthma and COPD using hyperpolarized  $^{129}\text{Xe}$  chemical shift saturation recovery spectroscopy and dissolved-phase MRI. *NMR Biomed*. 2014;27:1490–1501.
6. Ruan W, Zhong J, Wang K, et al. Detection of the mild emphysema by quantification of lung respiratory airways with hyperpolarized xenon diffusion MRI. *J Magn Reson Imaging*. 2016;45:879–888.
7. Ireland RH, Din OS, Swinscoe JA, et al. Detection of radiation-induced lung injury in non-small cell lung cancer patients using hyperpolarized  $^3\text{He}$  magnetic resonance imaging. *Radiother Oncol*. 2010;97:244–248.
8. Li H, Zhang Z, Zhao X, Sun X, Ye C, Zhou X. Quantitative evaluation of radiation-induced lung injury with hyperpolarized xenon magnetic resonance. *Magn Reson Med*. 2016;76:408–416.
9. Doganay O, Stirrat E, McKenzie C, Schulte RF, Santyr GE. Quantification of regional early stage gas exchange changes using hyperpolarized  $^{129}\text{Xe}$  MRI in a rat model of radiation-induced lung injury. *Med Phys*. 2016;43:2410–2420.
10. Mathew L, Vandyk J, Etemad-Rezai R, Rodrigues G, Parraga G. Hyperpolarized  $^3\text{He}$  pulmonary functional magnetic resonance imaging prior to radiation therapy. *Med Phys*. 2012;39:4284–4290.
11. Mathew L, Gaede S, Wheatley A, Etemad-Rezai R, Rodrigues GB, Parraga G. Detection of longitudinal lung structural and functional changes after diagnosis of radiation-induced lung injury using hyperpolarized  $^3\text{He}$  magnetic resonance imaging. *Med Phys*. 2010;37:22–31.
12. Virgincar RS, Cleveland ZI, Kaushik SS, et al. Quantitative analysis of hyperpolarized  $^{129}\text{Xe}$  ventilation imaging in healthy volunteers and subjects with chronic obstructive pulmonary disease. *NMR Biomed*. 2013;26:424–435.

13. Pike D, Kirby M, Guo F, McCormack DG, Parraga G. Ventilation heterogeneity in ex-smokers without airflow limitation. *Acad Radiol.* 2015;22:1068–1078.
14. Kirby M, Ouriadov A, Svenningsen S, et al. Hyperpolarized  $^3\text{He}$  and  $^{129}\text{Xe}$  magnetic resonance imaging apparent diffusion coefficients: physiological relevance in older never- and ex-smokers. *Physiol Rep.* 2014;2:e12068.
15. Diaz S, Casselbrant I, Piitulainen E, et al. Hyperpolarized  $^3\text{He}$  apparent diffusion coefficient MRI of the lung: reproducibility and volume dependency in healthy volunteers and patients with emphysema. *J Magn Reson Imaging.* 2008;27:763–770.
16. Wang C, Mugler JP 3rd, de Lange EE, Patrie JT, Mata JF, Altes TA. Lung injury induced by secondhand smoke exposure detected with hyperpolarized  $^3\text{He}$  diffusion MR. *J Magn Reson Imaging.* 2014;39:77–84.
17. Haefelibleuer B, Weibel ER. Morphometry of the human pulmonary acinus. *Anat Rec.* 1988;220:401–414.
18. Sukstanskii AL, Yablonskiy DA. In vivo lung morphometry with hyperpolarized  $^3\text{He}$  diffusion MRI: theoretical background. *J Magn Reson.* 2008;190:200–210.
19. Sukstanskii AL, Yablonskiy DA. Lung morphometry with hyperpolarized  $^{129}\text{Xe}$ : theoretical background. *Magn Reson Med.* 2012;67:856–866.
20. Yablonskiy DA, Sukstanskii AL, Leawoods JC, et al. Quantitative in vivo assessment of lung microstructure at the alveolar level with hyperpolarized  $^3\text{He}$  diffusion MRI. *Proc Natl Acad Sci USA.* 2002;99:3111–3116.
21. Paulin GA, Ouriadov A, Lessard E, Sheikh K, McCormack DG, Parraga G. Noninvasive quantification of alveolar morphometry in elderly never- and ex-smokers. *Physiol Rep.* 2015;3:e12583.
22. Yablonskiy DA, Sukstanskii AL, Quirk JD, Woods JC, Conradi MS. Probing lung microstructure with hyperpolarized noble gas diffusion MRI: theoretical models and experimental results. *Magn Reson Med.* 2014;71:486–505.
23. Quirk JD, Lutey BA, Gierada DS, et al. In vivo detection of acinar microstructural changes in early emphysema with  $^3\text{He}$  lung morphometry. *Radiology.* 2011;260:866–874.
24. Woods JC, Choong CK, Yablonskiy DA, et al. Hyperpolarized  $^3\text{He}$  diffusion MRI and histology in pulmonary emphysema. *Magn Reson Med.* 2006;56:1293–1300.
25. Hajari AJ, Yablonskiy DA, Sukstanskii AL, Quirk JD, Conradi MS, Woods JC. Morphometric changes in the human pulmonary acinus during inflation. *J Appl Physiol.* 2012;112:937–943.
26. Quirk JD, Chang YV, Yablonskiy DA. In vivo lung morphometry with hyperpolarized  $^3\text{He}$  diffusion MRI: reproducibility and the role of diffusion-sensitizing gradient direction. *Magn Reson Med.* 2015;73:1252–1257.
27. Quirk JD, Sukstanskii AL, Woods JC, Lutey BA, Conradi MS. Experimental evidence of age-related adaptive changes in human acinar airways. *J Appl Physiol.* 2016;120:159–165.
28. Ruppert K, Quirk JD, Mugler JP III, et al. Lung morphometry using hyperpolarized xenon-129: preliminary experience. *Proc Intl Soc Magn Reson Med.* 2012;20:1352.
29. Ouriadov A, Farag A, Kirby M, McCormack DG, Parraga G, Santyr GE. Lung morphometry using hyperpolarized  $^{129}\text{Xe}$  apparent diffusion coefficient anisotropy in chronic obstructive pulmonary disease. *Magn Reson Med.* 2013;70:1699–1706.
30. Donoho DL. Compressed sensing. *IEEE T Inform Theory.* 2006;52:1289–1306.
31. Candes EJ, Romberg J, Tao T. Robust uncertainty principles: exact signal reconstruction from highly incomplete frequency information. *IEEE T Inform Theory.* 2006;52:489–509.
32. Lustig M, Donoho D, Pauly JM. Sparse MRI: the application of compressed sensing for rapid MR imaging. *Magn Reson Med.* 2007;58:1182–1195.
33. Ajraoui S, Lee KJ, Deppe MH, Parnell SR, Parra-Robles J, Wild JM. Compressed sensing in hyperpolarized  $^3\text{He}$  lung MRI. *Magn Reson Med.* 2010;63:1059–1069.
34. Ajraoui S, Parra-Robles J, Wild JM. Incorporation of prior knowledge in compressed sensing for faster acquisition of hyperpolarized gas images. *Magn Reson Med.* 2013;69:360–369.
35. Qing K, Altes TA, Tustison NJ, et al. Rapid acquisition of  $^3\text{He}$  and proton three-dimensional image sets of the human lung in a single breath-hold using compressed sensing. *Magn Reson Med.* 2015;74:1110–1115.
36. Ajraoui S, Parra-Robles J, Marshall H, Deppe MH, Clemence M, Wild JM. Acquisition of  $^3\text{He}$  ventilation images, ADC,  $T_2^*$  and  $B_1$  maps in a single scan with compressed sensing. *NMR Biomed.* 2012;25:44–51.
37. Collier GJ, Wild JM. In vivo measurement of gas flow in human airways with hyperpolarized gas MRI and compressed sensing. *Magn Reson Med.* 2015;73:2255–2261.
38. Chan HF, Stewart NJ, Parra-Robles J, Collier GJ, Wild JM. Whole lung morphometry with 3D multiple b-value hyperpolarized gas MRI and compressed sensing. *Magn Reson Med.* 2017;77:1916–1925.
39. Wang N, Badar F, Xia Y. Compressed sensing in quantitative determination of GAG concentration in cartilage by microscopic MRI. *Magn Reson Med.* 2018;79:3163–3171.
40. Zhou X, Luo J, Sun XP, et al. Enhancement of solid-state proton NMR via the spin-polarization-induced nuclear overhauser effect with laser-polarized xenon. *Phys Rev B.* 2004;70:052405.
41. Sukstanskii AL, Bretthorst GL, Chang YV, Conradi MS, Yablonskiy DA. How accurately can the parameters from a model of anisotropic  $^3\text{He}$  gas diffusion in lung acinar airways be estimated? Bayesian view. *J Magn Reson.* 2007;184:62–71.
42. Hamedani H, Clapp JT, Kadlecck SJ, et al. Regional fractional ventilation by using multibreath wash-in  $^3\text{He}$  MR imaging. *Radiology.* 2016;279:917–924.
43. Chang YV, Quirk JD, Yablonskiy DA. In vivo lung morphometry with accelerated hyperpolarized  $^3\text{He}$  diffusion MRI: a preliminary study. *Magn Reson Med.* 2015;73:1609–1614.
44. Shanbhag DD, Altes TA, Miller GW, Mata JF, Knight-Scott J. Q-space analysis of lung morphometry in vivo with hyperpolarized  $^3\text{He}$  spectroscopy. *J Magn Reson Imaging.* 2006;24:84–94.
45. O'Halloran RL, Holmes JH, Wu YC, Alexander A, Fain SB.  $^3\text{He}$  MR q-space imaging with radial acquisition and iterative highly constrained back-projection. *Magn Reson Med.* 2010;63:41–50.
46. Juan PR, Helen M, Ruth AH, Christopher EB, Wild JM. Quantification of lung microstructure in asthma using a  $^3\text{He}$  fractional diffusion approach. *Proc Intl Soc Magn Reson Med.* 2014;22:3529.
47. Trampel R, Jensen JH, Lee RF, Kamenetskiy I, McGuinness G, Johnson G. Diffusional kurtosis imaging in the lung using hyperpolarized  $^3\text{He}$ . *Magn Reson Med.* 2006;56:733–737.
48. Ruan W, Zhong J, Guan Y, et al. Detection of smoke-induced pulmonary lesions by hyperpolarized  $^{129}\text{Xe}$  diffusion kurtosis imaging in rat models. *Magn Reson Med.* 2017;78:1891–1899.

# ClearCheck

## One-click plan evaluation



Dose Constraints • Plan Checks  
Structure Checks • Collision Checks